

CONTINUOUS VISUALIZATION OF NEARFIELD ACOUSTIC HOLOGRAPHY: A LABVIEW APPROACH

Rafael Santos Iwamura, rafael.iwamura@embraer.com.br

Thiago Matias de Carvalho, thiago.carvalho@embraer.com.br

Empresa Brasileira de Aeronáutica – São José dos Campos / Brazil

Cristiane Aparecida Martins, cmartins@ita.br

Instituto Tecnológico de Aeronáutica – São José dos Campos / Brazil

Jean-Hugh Thomas, jean-hugh.thomas@univ-lemans.fr

Laboratoire d'Acoustique de l'Université du Maine – Le Mans / France

Jean-Claude Pascal, jean-claude.pascal@univ-lemans.fr

Laboratoire d'Acoustique de l'Université du Maine – Le Mans / France

Abstract. *All the time we are exposed to sounds. There are some pleasant such as music but also unpleasant as aerotraffic noise. In both cases it is desired to obtain control over the present sound. This means that research into behavior of sound sources is fundamental. Near-field Acoustic Holograph (NAH) is considered an important part in this research. With NAH it possible to visualize and even propagate sound-fields to any desired plane via pressure measurements in the near-field of sound sources. Description of the NAH theory, as other radiation problems, has its basis on the solution of the Helmholtz equation, whose result is a complex pressure field. This has been the subject of several studies which proposed different approaches of the NAH theory, usually dedicated to stationary events. However many industrial applications require processing in the time domain for moving source pass-by noise or time-evolving system analysis. Typically the treatment involves the wave-number domain, where filtering makes it accurate, and a real-time visualization of the wave-number spectrum would be helpful to better understanding the phenomena. The aim of this work is to describe how the theory of NAH in current use may be implemented in a LabVIEW™ environment in order to obtain a continuous visualization of the pressure field on the source plane.*

Keywords: *Aeroacoustics, Nearfield Acoustic Holography, real-time processing, wavenumber domain, LabVIEW™ programming*

1. INTRODUCTION

Noise level has become an important issue in current projects of the transportation industry. The legislation in most of the countries has been increasingly severe with the emitted noise level, aiming to enhance comfort and quality of life to operators, customers and people who live nearby the operational sites. In some fields, such as aeronautical, the concern with noise levels should override the legislation searching for quieter products, an important factor of selection to airliners and other customers.

In this context, acoustics is present on two fronts: first, in the aircraft design, when, for instance, selected parts of the structure are reinforced to reduce vibration and hence noise levels; second, in the improvement of a product, seeking to identify and locate unpredicted noise sources. The latter, related to this work, is usually addressed by imaging methods that differ in accuracy and cost. Zani (2003) describes the main methods available today, which are summarized in Table 1, transcribed from the same reference.

Williams *et al.* (2000) explores in interesting way an application of holography in revealing sound-transmission paths from the engine to the interior space of a turboprop airplane. The study is performed through the determination of the normal velocity over a large area of the aircraft fuselage.

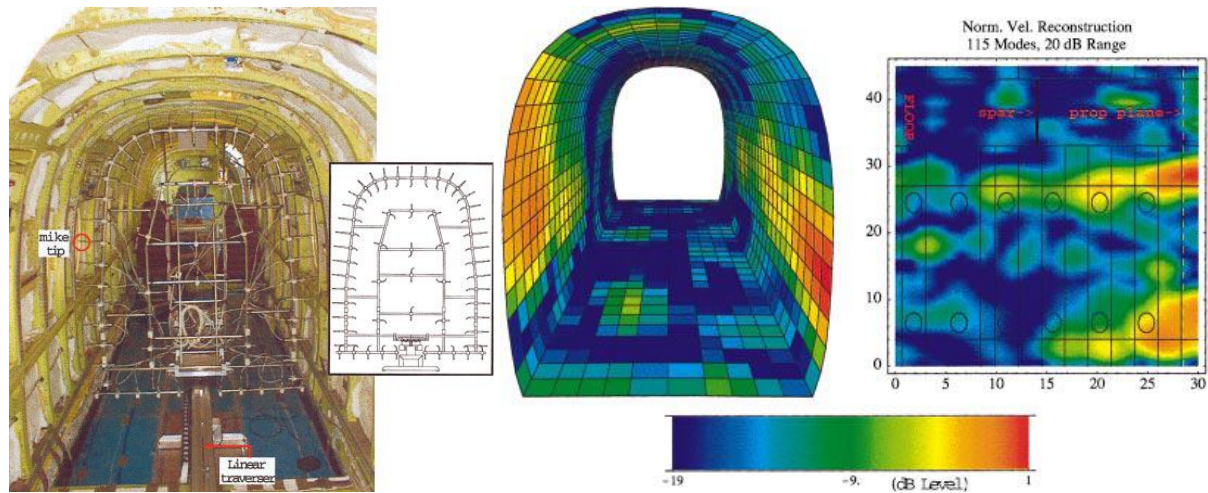


Figure 1: Aeronautical application of NAH – Willians *et al.* (2000)

Table 1: Major acoustic imaging methods according to Zani (2003).

	Main advantages	Main limitations	Privileged application field
Pressure cartography	<ul style="list-style-type: none"> - Simple and low cost method - Wide range of frequencies (a few hertz to tens of kHz) 	<ul style="list-style-type: none"> - Very low resolution - Requires long time acquisition - Not convenient unless for stationary sources 	<ul style="list-style-type: none"> - Method little widespread - Not convenient unless for measurements on anechoic chamber
Intensimetry	<ul style="list-style-type: none"> - Fairly high resolution - Low cost method - Wide range of frequencies (250Hz – 3kHz) 	<ul style="list-style-type: none"> - Provides the noise level at a distance of the object (rather than at the source) - Fairly long acquisition (point by point) - Not convenient unless for stationary sources 	Buildings, automobile, measures in transmission (tests of acoustic transparency) Calculation of sound power
Beam-forming	<ul style="list-style-type: none"> - High resolution in high frequencies - Wide range of frequencies (up to 20kHz) - Functional for stationary sources or not - Quick measures 	<ul style="list-style-type: none"> - Measures of relative levels - Low resolution at low frequencies. 	Tests of complete vehicles in wind tunnel, outdoors mapping, in long distance from the object, location of mobile sources (airplanes in flight, noise passage of trains, etc.)
Stationary holography	<ul style="list-style-type: none"> - High resolution - Fast computation of many parameters (Pressure, power, speed, intensity, etc.) 	<ul style="list-style-type: none"> - Expensive method - Limited to stationary sources 	Automobile Calculation of sound power
Non-stationary holography	<ul style="list-style-type: none"> - High resolution - Functional for stationary sources or not - Fast computation of many parameters (Pressure, power, speed, intensity, etc.) - Provides mapping at every moment (8192 times per second, for example) 	<ul style="list-style-type: none"> - Expensive method - Requires a large number of microphones 	Engine on test bench Cartography readjustment with respect to the crankshaft angle Calculation of sound power

This article describe how the theory of NAH, usually dedicated to stationary events, may be explored in current computational environments to study non-stationary phenomena. The routine was developed in LabVIEW™ and is able to reconstruct the acoustic pressure field on the source plane continuously over the time, allowing variations in the sources to be perceived almost instantly. In this approach, all the data processing is performed in the wavenumber domain and brought to the time domain only to be displayed on the screen.

2. THEORETICAL DEVELOPMENT

A detailed development of the theory of NAH may be found in Maynard (1985), as well as in Veronesi and Maynard (1987). This section aims to summarize the main points employed in the developed of the proposed routine.

NAH involves finding the solution for the Helmholtz equation [Eq. (1)] with a specified Dirichlet ψ_D or Neumann ψ_N boundary condition. As a simplification, the present work uses $\psi_D(x,y)$ on the plane $z = 0$ as the boundary condition. Therefore, the solution of the Helmholtz equation is a two-dimensional convolution integral presented in Eq. (2) with Green's function (G_D), for an infinite plane boundary, given by Eq. (3).

$$\nabla^2 \psi + k^2 \psi = 0, \text{ with } k = 2\pi/\lambda, \text{ where } \lambda \text{ is the characteristic wavelength of the radiation} \quad (1)$$

$$\psi(x, y, z) = \iint_{-\infty}^{\infty} \psi_D(x', y') G_D(x - x', y - y', z) dx' dy' \quad (2)$$

$$G_D(x, y, z) = z(1 - ikR) e^{ikR} / 2\pi R^3, \text{ where } R = \sqrt{x^2 + y^2 + z^2}. \quad (3)$$

Since the domain (k_x, k_y) is referred to a k space, and (x,y) is in real space, the application of convolution theorem to Eq. (2), using Fourier and inverse Fourier transforms, resumes to the expression for the pressure field, given by Eq. (4). The continuous, infinite two-dimensional Fourier transform of a function $f(x,y)$ is given by Eq. (5) and its inverse is indicated by F^{-1} .

$$\psi(x, y, z) = F^{-1}[\hat{\psi}_D(k_x, k_y) \hat{G}_D(k_x, k_y, z)] \quad (4)$$

$$\hat{f}(k_x, k_y) = \iint_{-\infty}^{\infty} f(x, y) e^{-i(k_x x + k_y y)} dx dy \quad (5)$$

The Fourier transform of G_D in Eq. (3) is obtained analytically and resumes to Eq. (6)

$$\hat{G}_D(k_x, k_y, z) = \begin{cases} \exp(iz\sqrt{k^2 - k_x^2 - k_y^2}), & k_x^2 + k_y^2 \leq k^2 \\ \exp(-z\sqrt{k_x^2 + k_y^2 - k^2}) & k_x^2 + k_y^2 > k^2 \end{cases} \quad (6)$$

It is observed that points (k_x, k_y) outside the radiation circle, given by $k^2 = k_x^2 + k_y^2$, indicates an exponential decay of evanescent waves, while points inside the radiation circle indicates the z -direction phase change of propagation plane waves. Assuming that $\psi(x,y,z_H)$ is known, Eq. (7) is developed and allows the reconstruction of the evanescent and propagating waves.

$$\psi_D(x, y) = F^{-1}[\hat{\psi}(k_x, k_y, z_H) \hat{G}_D^{-1}(k_x, k_y, z_H)] \quad (7)$$

According to Veronesi and Maynard (1987), "Once the source field ψ_D has been determined, all other properties of the field may be calculated [...]. It should be noted that [...] $\psi_D(x,y)$ need not correspond to a physical source surface." Actually, it is possible to generalize to the field between any two planes, one at z and the other at z_0 located between zero (source plane) and z , the two-dimensional convolution integral, given by Eq. (2), therefore,

$$\psi(x, y, z) = \iint_{-\infty}^{\infty} \psi(x', y', z_0) G_D(x - x', y - y', z - z_0) dx' dy' \quad (8)$$

"Since $z > z_0 > 0$ and zero is the actual source plane, then the reconstruction processes may be referred to as the inverse propagation of a wavefront back toward the source." (Veronesi and Maynard, 1987)

2.1. Finite and discrete conditions

The formulation previously described for the NAH problem assumes infinite planes and continuous fields. However, numerical evaluation of the formulas related to Fourier transforms, Eq. (2) or Eq. (5), requires finite, discrete operations, whose limitations are evaluated either by experimental data acquisition or by computation time and capacity. To make the numerical computation possible, some assumptions must be made.

First, the sources of the wavefield are such that the boundary data $\psi_D(x,y)$ are negligible outside of some finite domain $(-L/2 < x < L/2$ and $-L/2 < y < L/2)$ in real space, reading to Eq. (9).

$$\psi(x, y, z) \approx \iint_{-L/2}^{L/2} \psi_D(x', y') G_D(x - x', y - y', z) dx' dy' \quad (9)$$

As a second assumption, the pressure field ψ may be well described with a discrete, as well as finite, set of numbers. This can be “a data set from experimental measurements at lattice points in real space or the coefficients of a superposition of basis functions” (Veronesi and Maynard, 1987). We adopt in this work that the LxL real space domain is shared into N^2 patches of size $(L/N)x(L/N)$, labeled with integers $l, m = 0, 1, \dots, N-1$, and “the discrete set of data $\psi_D(l, m)$ is assumed to be the average of the actual boundary field over the patch” (Veronesi and Maynard, 1987). Following the assumption of the previous paragraph, Eq. (9) reads:

$$\psi(x, y, z) = \sum_{l=0}^{N-1} \sum_{m=0}^{N-1} \psi_D(l, m) \int_{x_l - \Delta/2}^{x_l + \Delta/2} \int_{y_m - \Delta/2}^{y_m + \Delta/2} G_D(x - x', y - y', z) dx' dy' \quad (10)$$

$$x_l = (l + 1/2 - N/2)\Delta, \text{ where } \Delta = L/N. \quad (11)$$

$$y_m = (m + 1/2 - N/2)\Delta, \text{ where } \Delta = L/N. \quad (12)$$

Finally we assume it is sufficient to evaluate the field ψ in any plane z at discrete points (x_p, y_q) , defined by Eq. (10) for integers $p, q = 0, \dots, N-1$. Also, defining variables $u = x_p - x$, $v = y_q - y$, Eq. (13) is obtained with integers $l, m, p, q = 0, \dots, N-1$. For $\psi(x, y, z) = \psi(x_p, y_q, z)$, the radiated field may be expressed by Eq. (14), which is the discrete and finite version of the Rayleigh integral [Eq. (1)].

$$\int_{x_l - \Delta/2}^{x_l + \Delta/2} \int_{y_m - \Delta/2}^{y_m + \Delta/2} G_D(x_p - x', y_q - y', z) dx' dy' = \int_{(p-l-1/2)\Delta}^{(p-l+1/2)\Delta} \int_{(q-m-1/2)\Delta}^{(q-m+1/2)\Delta} G_D(u, v, z) dudv \equiv \bar{G}_D(p-l, q-m, z) \quad (13)$$

$$\psi(p, q, z) = \sum_{l=0}^{N-1} \sum_{m=0}^{N-1} \psi_D(l, m) \bar{G}_D(p-l, q-m, z) \quad (14)$$

The discrete convolution in Eq. (14) is readily evaluated and inverted using the convolution theorem and Fourier transform (usually the Fast Fourier Transform algorithm). Most treatments of the discrete, finite convolution theorem assume that both arrays to be convolved are either periodic or zero for indices outside the range $0, \dots, N-1$. However, in the discrete convolution in Eq. (14), one of the arrays, $\bar{G}_D(p-l, q-m, z)$ [Eq. (13)] may be evaluated for all integers l, m, p, q , once the Green's function $G_D(u, v, z)$ may be analytically obtained over an infinite domain. Concerning this feature, the discrete convolution theorem can be modified to extend the sequence $\psi'_D(l, m)$, which is defined only for integers (l, m) in $(0, N-1)$, over a $(2N)x(2N)$ domain, by adding zeros (process know as *Zero Padding*). Hence the new sequence reads:

$$\psi'_D(l, m) = \begin{cases} \psi_D(l, m), & \text{if } 0 \leq l < N \text{ and } 0 \leq m < N \\ 0, & \text{if } N \leq l < 2N \text{ and } N \leq m < 2N \end{cases} \quad (15)$$

The discrete Fourier transform $DFT\{f\}$ of array (l, m) in $(0, 2N-1)$ is defined (for $\mu, \nu = 0, 1, \dots, 2N-1$) by Eq. (16) and its inverse expressed by Eq. (17).

$$DFT\{f\}_{\mu, \nu} = \sum_{l=0}^{2N-1} \sum_{m=0}^{2N-1} f(l, m) e^{-i(\pi/N)(l\mu + m\nu)} \quad (16)$$

$$IDFT\{F\}_{l, m} = \frac{1}{4N^2} \sum_{\mu=0}^{2N-1} \sum_{\nu=0}^{2N-1} F(\mu, \nu) e^{-i(\pi/N)(l\mu + m\nu)} \quad (17)$$

Thus, the finite discrete convolution (14) reads to Eq. (18) Where \bar{G}'_D is given by Eq. (19).

$$\psi(p, q, z) = IDFT[DFT\{\psi'_D\}DFT\{\bar{G}'_D(z)\}] \quad (18)$$

$$\bar{G}'_D(l, m, z) = \begin{cases} \bar{G}_D(l, m, z) & \text{if } 0 \leq l < N \text{ and } 0 \leq m < N \\ \bar{G}_D(l-2N, m, z) & \text{if } N \leq l < 2N \text{ and } 0 \leq m < N \\ \bar{G}_D(l, m-2N, z) & \text{if } 0 \leq l < N \text{ and } N \leq m < 2N \\ \bar{G}_D(l-2N, m-2N, z) & \text{if } N \leq l < 2N \text{ and } N \leq m < 2N \end{cases} \quad (19)$$

2.3. Application

In order to simplify the problem formulation, the projection (z_F), the hologram (z_H), and the source (z_S) planes are, initially, considered infinite and continuous. The assumption of $z_H = z_S$ can also be made, with the holographic images showing the reconstructed pressure field on the source plane. Hence, as input data to the program, the function $\psi(x, y, z_H, t)$ is given as function of time and position (x, y) on the hologram plane (z_H).

The next steps consist in applying a Fourier Transform, to obtain ψ in the frequency domain – Eq. (20) – and a 2D spatial Fourier Transform over a selected frequency (ω_0), taking the function from spatial domain (x, y) into the wavenumber domain (k_x, k_y), as presented in Eq. (21)

$$\hat{\psi}(x, y, z_F, \omega) = \int_0^{\infty} \psi(x, y, z_F, t) e^{i\omega t} dt \quad (20)$$

$$\bar{\psi}(k_x, k_y, z_F, \omega_0) = F_{2D}(x, y, z_F, \omega_0) = \int_{-\infty}^{\infty} \int_{-\infty}^{\infty} \hat{\psi}(x, y, z_F, \omega_0) e^{-i(k_x x + k_y y)} dx dy \quad (21)$$

Then the propagation from the z_F to the z_S can be evaluated using the Green's function $G(k_r, d, \omega_0)$, and since $z_H = z_S$, we obtain Eq. (22) where d is the distance between the planes and the wavenumber k_z is given by Eq. (23)

$$\bar{\psi}(k_x, k_y, z_F, \omega_0) = \bar{\psi}(k_x, k_y, z_S, \omega_0) \exp(+ik_z d) = \bar{\psi}(k_x, k_y, z_S, \omega_0) G(k_r, d, \omega_0) \quad (22)$$

$$k_z^2 = k_0^2 - k_r^2 = k_0^2 - (k_x^2 + k_y^2) \quad (23)$$

Green's function depends on the relation between the values of k_r and k_0 . If k_r is larger than k_0 , we have $G(k_r, d, \omega_0)$ as a real exponential equation, related to the evanescent waves. Otherwise, Green's function is a complex exponential, which behaves as a sinusoidal function, related to the propagating waves. This can be expressed as,

$$G(k_r, d, \omega_0) = \begin{cases} \exp\left(id\sqrt{k^2 - k_r^2}\right), k_r \leq k \\ \exp\left(-d\sqrt{k_r^2 - k^2}\right), k_r > k \end{cases} \quad (24)$$

However, what concerns for the pressure field reconstruction is the inverse propagation of the data from z_H to the plane of source z_S . This is obtained using the inverse Green's function:

$$\bar{\psi}(k_x, k_y, z_S, \omega_0) = \frac{\bar{\psi}(k_x, k_y, z_F, \omega_0)}{G(k_r, d, \omega_0)} = \bar{\psi}(k_x, k_y, z_F, \omega_0) G^{-1}(k_r, d, \omega_0) \quad (25)$$

A filter is added to reduce the influence of evanescent waves with very intense values, using a Veronesi's filter, which depends on the relation between values of k_r and a parameter k_c chosen by the user, with typical value $k_c = 0,6k_{max}$. This can be expressed as:

$$\bar{\psi}(x, y, z_S, \omega_0) = W(k_r) \bar{\psi}(k_x, k_y, z_F, \omega_0) G^{-1}(k_r, d, \omega_0) \quad (26)$$

$$W(k_r) = \begin{cases} 1 - \frac{\exp((k_r/k_c - 1)/\alpha)}{2}, & k_r \leq k_c \\ \frac{\exp((1 - k_r/k_c)/\alpha)}{2}, & k_r > k_c \end{cases} \quad (27)$$

Now that we have the data filtered and already treated with the inverse propagation, it is possible to submit $\bar{\psi}(k_x, k_y, z_s, \omega_0)$ to an inverse SFT-2D, giving the pressure field on the source plane, namely, the holographic images, represented here by,

$$\hat{\psi}(x, y, z_s, \omega_0) = F_{2D}^{-1}(x, y, z_s, \omega_0) = \int \int_{-\infty}^{\infty} \bar{\psi}(k_x, k_y, z_s, \omega_0) e^{+i(k_x x + k_y y)} dk_x dk_y \quad (28)$$

Equation (26) shows that the Veronesi's filter and Green's function are expressions that multiply the function $\bar{\psi}(k_x, k_y, z_s, \omega_0)$. It seems, at least theoretically, the order in which the two terms are inserted in the expression is not important. However, the routine built in LabVIEW first presents the filter signal, and then makes the inverse propagation. This is the sequence shown in Figure 2.

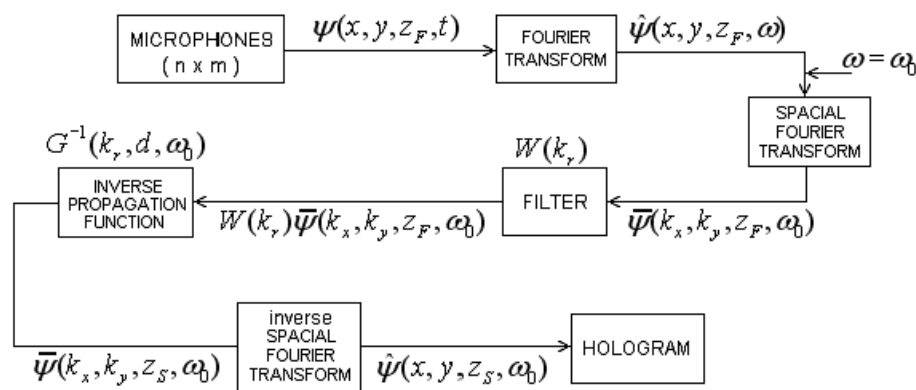


Figure 2: Program block diagram for each holographic image.

All the steps given in Figure 2 are related to one holographic image, this is why all the theory previously described is the same as for stationary NAH. It means that the “illusion” of continuity is produced by showing several images of stationary NAH in a short period of time.

3. PROGRAM IMPLEMENTATION

Let us start describing the main part of the program (“kernel”) that executes the manipulation of the acquired signal in the wavenumber domain. It is related to Eq. (7), being responsible for filtering (*Veronesi*, *Tikhonov*, etc) and inverse propagation processes (Green's function). The last one leads to the reconstruction of the wavenumber spectra on the source plane and is characterized by a function in space that multiplies the signal already filtered, regarding whether the wave is propagating or evanescent. All this is exemplified by the “data treatment” box in Figure 3, which also shows the main steps between the acquired signal and the holographic image in a simple manner.



Figure 3: Sketch showing the data treatment (kernel) layout and some primary tools suitable to the solution of the holographic image visualization.

Initially a Short-time Fourier Transform (STFT) is performed over the signal, followed by a Fast Fourier Transform (FFT), the data treatment, and eventually by another space transformation (inverse FFT), after which it is possible to visualize the holographic images. The idea is to take data from time domain into wavenumber domain, where the kernel is evaluated, and return to exhibit the complex pressure field on the source plane. It is important to remind that while the STFT is executed over the signal of each microphone, the FFT is over the signal of the antenna as a whole (Spatial Fourier Transform) and it is performed for a pre-defined frequency.

Differently of what was exposed in item 2, the source and measurement planes are considered finite and discrete. The FFT function of LabVIEW is capable to perform properly the discrete transformation. However it is interesting to attenuate the discretization on the exhibition of holographic image, which is performed here through data interpolation. Also it is necessary to smooth the effects of truncated information (Veronesi and Maynard, 1987 as well as Pascal, 2005). That is carried out by adding a mesh of zeros around the data of the measurement plane (zero padding). Figure 4 gives a more complete diagram of the process executed by the routine.

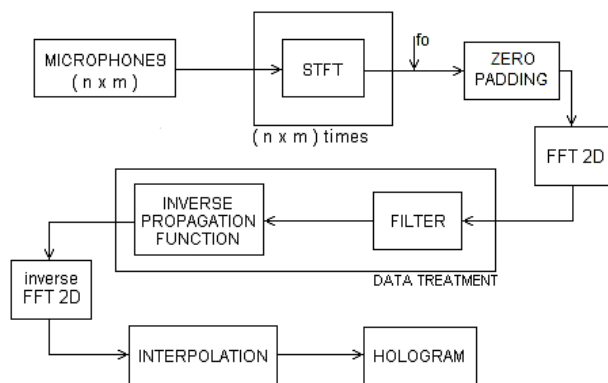


Figure 4: Program block diagram for each holographic image.

As previously stated, the routine performs the NAH process in sequence. This way, the whole structure described in Figure 4 is inside a *while* routine, so that each loop receives the signal acquired and return a holographic image. What makes the visualization looks like a “time-continuous” one is the rate of images plotted, i.e., how fast a loop is closed.

Iwamura and Matias (2007) describes in details the routine developed, assessing the resources available in the LabVIEW™ environment and the approaches employed.

4. RESULTS AND DISCUSSIONS

The routine was developed to acquire, process and display data almost in real time. As it was not possible to set up an experimental arrangement to test the routine developed, we propose some numerically experiments to verify the program capacities.

However, building a source function to simulate the acquisition data in NAH is not as evident as it might seem at the beginning. Some features, as the distance between the source and each microphone, must be calculated, as well as phase changing, due to a different time-delay depending on the microphone position in the mesh.

The available source signal is based on a sinusoidal signal conformed by a hyperbolic secant function. The hyperbolic secant function was chosen because it is a decreasing curve similar to a negative exponential one, with the advantage of being an even function with a smaller derivative. The signal read by the microphones from each source is expressed by Eq. (29) where (x, y) are the microphone location on the antenna plane.

$$S(x, y) = \frac{\sin[2\pi f \cdot (t - t_0)]}{R(x, y)} \cdot \text{sech} \left[\lambda \left(t - t_0 - \frac{R(x, y)}{c} \right) \right] \quad (29)$$

Term t_0 in Eq. (29) is equal to the initial delay, defined in the program as 7s. The third term in the secant function is related to the position of the microphone in the antenna, and $R(x, y)$ is the distance between the microphone and the source. Two sources are employed in the tests simulating signal emission for a squared array of 256 microphones displaced 8 cm from the source. Tests were run in a PC Pentium® IV with 512 Mb of available RAM memory.

4.1. Influence of Veronesi Filter

The theory of NAH succeeds in achieving a resolution greater than other stationary methods due to the processing of evanescent waves. However it is necessary to control the signal retropropagation to avoid the amplification of interferences on the measurements. In this work it was chosen the Veronesi filter to work on this topic. According to Pascal (2005a), filtering parameters are usually determined experimentally and only recently some methods have been proposed to determine them automatically (Williams, 2001).

The next two figures correspond to a pair of sources located at (0,2;0,4) and (0,3;0,3), delayed 2s. Figure 5 shows the acoustic pressure field on the antenna plan and on the source plan, without any filtering process and taken almost in the same instant of the previous figures $t \approx 5,4s$. The hologram of the field retropropagated permits to identify clearly the two noise sources; however, the pressure amplitude on the source plan is almost 17 times higher than pressure on measurement plan, which is positioned only 6 cm ahead. These results corroborate with the statement of filtering necessity.

It is observed the similarity among the images and, at the same time, the great differences in the amplitude values. In fact, the similarity is consequence of the amplitude limits adjustments and a calibration is necessary to determine the best filtering parameters. Here it is not possible to point the more adequate parameters, but Figure 5 to Figure 7 will give an idea of how filtering influence the results.

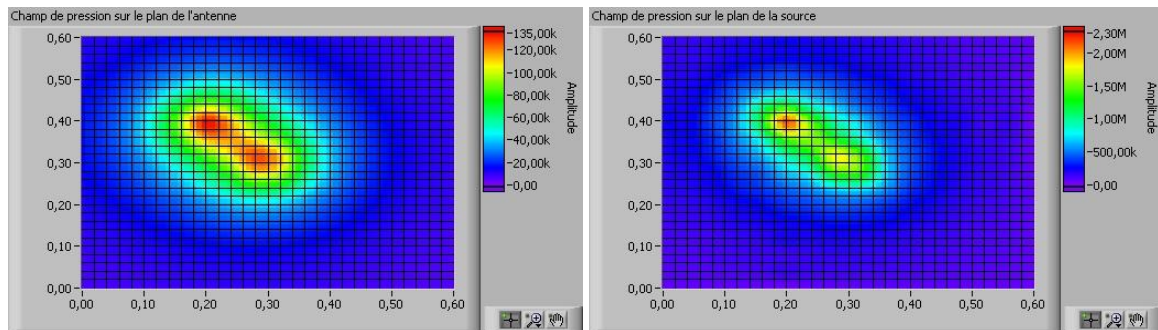


Figure 5: Pressure field on the antenna plan and on the source plan without filtering.

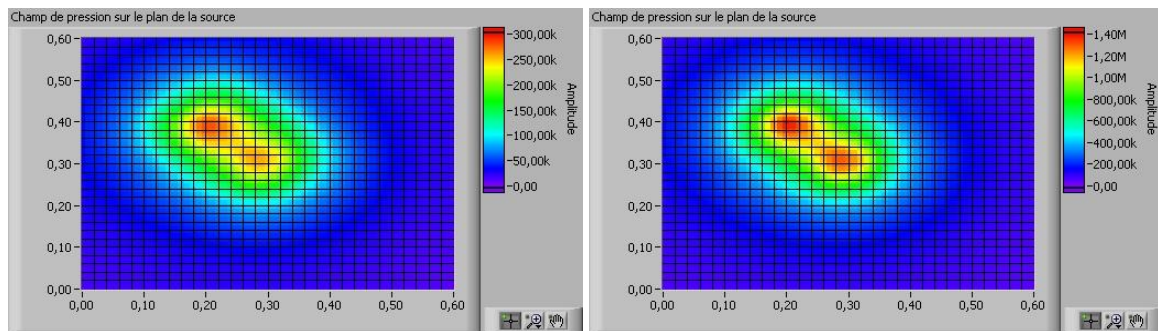


Figure 6: Pressure field on the source plan, for $kc = 0,6k\text{m}\acute{a}x$ and $S = 0,2$ (Left)
 Pressure field on the source plan, for $kc = 0,89k\text{m}\acute{a}x$ and $S = 0,2$ (Right).

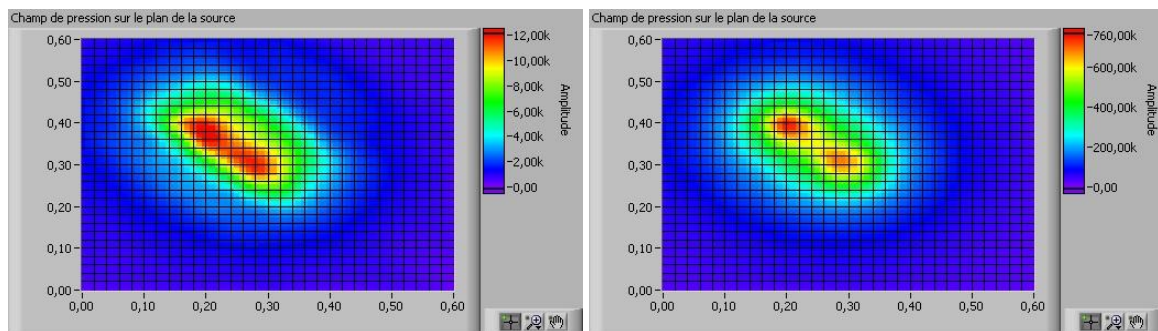


Figure 7: Pressure field on the source plan, for $kc = 0,39k\text{m}\acute{a}x$ and $S = 0,22$ (Left).
 Pressure field on the source plan, for $k = 0,6k\text{m}\acute{a}x$ and $S = 0,9$ (Right).

4.2. Influence of the parameter of the STFT function

Developing a STFT function specifically was considered beyond the scope of this work and the STFT function available in LabVIEW™ is employed (see Iwamura and Matias (2007) for more information)

Some input parameters are requested to define the window and sampling of the STFT. Generally, the higher are the values of these parameters the lower is the processing speed. The window type does not seem to interfere much in the processing and throughout the tests the rectangular window was used, since it is the simplest one.

The greatest differences on time-processing occurs when time-increment is decreased without changing the window length or the opposite, increasing window length without increasing the time-increment proportionally. The frequency interval also increases considerably the time-processing. Doubling its value would result, for instance, in a time-processing 10% higher. We have successfully used a simple rule to define these parameters: the frequency interval was half of the time increment and this was half of the window length.

The quality of the results should decrease only when the length window or the frequency interval is reduced to a few tens. However the amplitude may vary with the parameters and would require different calibrations.

Eventually, Pascal (2005a) suggests the utilization of Hanning window to perform the STFT in order to avoid distortions. Though, a further study would be necessary to determine the influence of window type in this routine. Figure 8 brings the same configuration of the hologram of Figure 6 for comparison.

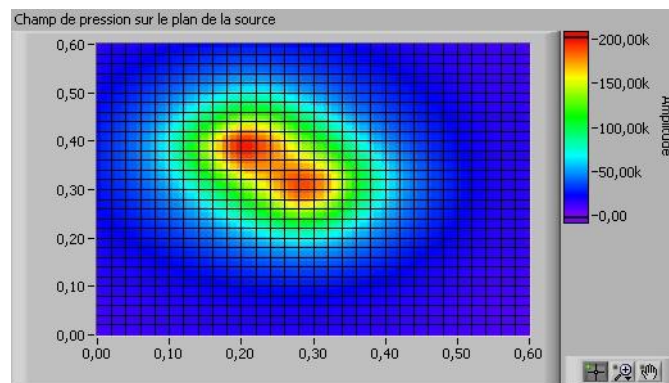


Figure 8: Hologram produced utilizing a Hanning window. Instant $t \approx 5,4s$, $kc = 0,6kmáx$ and $S = 0,2$.

4.3. Boundary effects

The application of zero padding is intended to minimize processing errors due to data discretization and finite aperture of the hologram. These are named Wraparound error by Maynard (1985). Here some distortions on positioning a source on the boundary of the hologram are illustrated in Figure 9. Other boundary effects due to the pressure field truncation, not approached here, are illustrated in Pascal (2005a). A method to deal with these errors is proposed in Thomas and Pascal (2005) and may be easily implement in the routine.

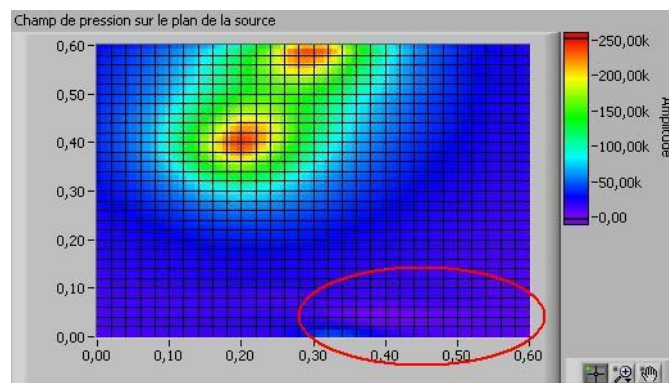


Figure 9: Distortions due to the boundary effects circled in red.

5. FINAL CONSIDERATIONS

The numerical tests performed indicate the routine is already adequate to run experimental trials. Little modifications will be necessary to include the acquisition subroutine and to adjust its output data to the format compatible to the rest of the program. Maynard (1985), Bös and Kurtza (2005) might be useful for designing the microphone array and setting the experimental arrangement.

The STFT function might be rewritten to optimize the visualization frame rate, which currently is about 10 images per second without using interpolation. The interpolation tool is another function that could be developed specifically for this routine in order to enhance its performance. Other improvements that could be implemented are a subroutine to save input data for future studying or even processing, an indicator of frequency spectrum captured by the microphones and an interface that allowed modifying the selected frequency while acquiring data. That would require calculating the green and the filtering matrices during the data processing, what may decrease the image frame rate if not well implemented.

Eventually calculation of other parameters of the acoustic field (*e.g.* power, magnitude and speed) as well as filters (Tikhonov) could be added. This could increase the utility of the program for areas beyond the acoustics, such as materials and structural dynamics. The efforts to develop the routine in modules will also contribute to simplify the implementation of these modifications.

6. LIST OF ABBREVIATIONS

DFT	Discrete Fourier Transform	SFT	Spatial Fourier Transform
FFT	Fast Fourier Transform	STFT	Short-Time Fourier Transform
IDFT	Inverse Discrete Fourier Transform	TC-NAH	Time Continuous Nearfield Acoustic Holograph
NAH	Nearfield Acoustic Holograph		
RT-NAH	Real-Time Nearfield Acoustic Holograph		

7. ACKNOWLEDGMENTS

We would like to grant in memoriam the outstanding support of Professor Dr. Maher Nasr Bismarck-Nasr for the accomplishment of this work.

8. REFERENCES

- Bös, J. and Kurtze, L., 2004, "Design And Application Of A Low-Cost Microphone Array For Nearfield Acoustical Holography". Technische Universität Darmstadt (Germany).
- Iwamura, R. S. and Carvalho, T. M., 2007, "Continuous Visualization of Nearfield Acoustic Holography: a LabVIEW Approach", Instituto Tecnológico de Aeronáutica – ITA, São José dos Campos (Brazil).
- Maynard, J. D., Williams, E. G. and Lee, 1985, Y. "Nearfield Acoustic Holography: I. Theory Of Generalized Holography And The Development Of Nah", Journal Of Acoustical Society Of America 78, 1395-1413.
- Pascal, J. C., 2005a, "Introduction A La Technique D'holographie Acoustique" Institut Pour La Promotion Des Sciences De L'ingénieur (Ipsi), Paris (France).
- Pascal, J. C., 2005b, "Application De L'holographie Acoustique Et Autres Techniques De Localisation De Sources" Institut Pour La Promotion Des Sciences De L'ingénieur (Ipsi), Paris (France).
- Thomas, J.-H., Grulier, V., Paillasseur, S. and Pascal, J.-C., 2006, "Rt-Nah: A Nearfield Acoustic Holography Technique For Real-Time Reconstruction". Euronoise 2006, Tampere (Finland).
- Thomas, J.-H. and Pascal, J. C., 2005, "Wavelet Preprocessing For Lessening Truncation Effects In Nearfield Acoustical Holography". Journal Of Acoustical Society Of America 118, 851-860.
- Veronesi, W.A. and Maynard, J. D., 1987, "Nearfield Acoustical Holography (Nah): Ii. Holographic Reconstruction Algorithms And Computer Implementation", Journal Of Acoustical Society Of America 81, 1307-1322.
- Williams, E. G., Houston, B. H., Herdic, P. C., Raveendra, S. T. and Gardner, B., 2000, "Interior Near-Field Acoustical Holography In Flight". Journal Of Acoustical Society Of America 108, 1451-1463.
- Williams, E. G., 2001, "Regularization Methods For Near-Field Acoustical Holography" Journal Of Acoustical Society Of America 110, 1976-1988.
- Zani, M.-L., 2003, "L'holographie Acoustique, Un Retour Aux Sources... De Bruit !". Revue Mesures, Ed. 755, Pg 49-52 (Mai).

9. RESPONSABILITY NOTICE

The authors are the only responsible for the printed material included in this paper.